CHEMISTRY OF MATERIALS

pubs.acs.org/cm Article

Pushing the Limits of Metastability in Semiconducting Perovskite Oxides for Visible-Light-Driven Water Oxidation

Shaun O'Donnell, Ching-Chang Chung, Abigail Carbone, Rachel Broughton, Jacob L. Jones, and Paul A. Maggard*

Cite This: *Chem. Mater.* 2020, 32, 3054–3064 Read Online

ACCESS | Metrics & More | Article Recommendations | Supporting Information

ABSTRACT: A synthetic route has been discovered to thermodynamically unstable, i.e., metastable, Sn(II)−perovskite oxides that have been highly sought after as lead-free dielectrics and small bandgap semiconductors. A highly facile exchange of Sn(II) is found by using a low melting $SnCl_2/SnF_2$ peritectic flux, yielding mixed A-site $(Ba_{1-x}Sn_x)ZrO_3$ and mixed A- and B-site $(Ba_{1-x}Sn_x)(Zr_{1-y}Ti_y)O_3$ solid solutions that exhibit a very high metastability, with up to 60% Sn(II) cations and a calculated reaction energy for decomposition of up to −0.3 eV atom^{-1}. Kinetic stabilization of the higher Sn(II) concentrations is achieved by the high cohesive energy of the perovskite compositions containing Zr(IV) and mixed Zr(IV)/Ti(IV) cations. Significantly red-shifted bandgaps are found with increasing Sn(II) substitution, enabling the optical absorption edge to be broadly tuned from ∼3.90 to ∼1.95 eV. Percolation pathways are calculated to occur for BSZT compositions with >12.5% Sn(II) and >25% Ti(IV) cations. High photocatalytic rates are found for molecular oxygen production for compositions which exceed the percolation thresholds, wherein extended diffusion pathways should "open up" across the structure and the charge carriers become delocalized rather than trapped. These results establish the critical importance of synthetically accessing metastable semiconductors for the discovery of advanced optical and photocatalytic properties.

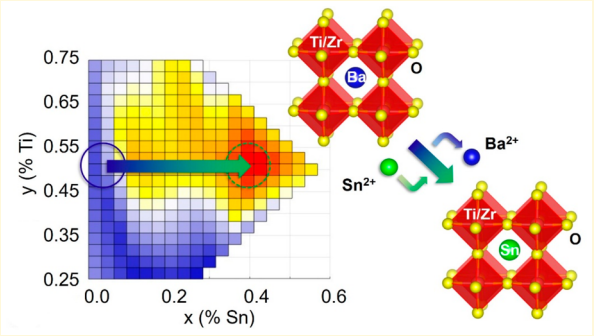

1. INTRODUCTION

Research into Sn(II)-containing semiconductors has garnered significant interest because of their potential technological importance, such as within the fields of solar energy conversion, ferroelectrics, and transparent conducting oxides (TCOs).[1−3] Intriguing optical properties of Sn(II)-containing oxides include their small semiconducting bandgaps, e.g., ∼1.6 to 2.0 eV, as a result of the high energy valence band formed by the filled O 2p/Sn 5s states. These semiconductors can also commonly exhibit a large valence band dispersion originating from the extended −O−Sn−O−Sn− connectivity and coordination geometries. Consequently, relatively low effective masses and high carrier mobilities are achievable, as highly desired in semiconductor applications such as in photovoltaics, photocatalysis, and TCOs. In the field of ferroelectrics, the perovskite-type $SnTiO_3$, $Sn(Zr_{0.5}Ti_{0.5})O_3$, and related phases have been intensely investigated as Pb-free, isoelectronic versions of $PbTiO_3$ and $Pb(Zr_{0.5}Ti_{0.5})O_3$.[4−8] The latter perovskite is one of the most widely used ceramics in the electronics industry because of its strong piezoelectric effect. Prior computational studies on the structure of $SnTiO_3$ have posited the occurrence of a very high ferroelectric polarization (∼1.1 C m^{-2}), resulting from a stronger tetragonal distortion as compared to $PbTiO_3$.[6,7] However, the bulk syntheses of $SnTiO_3$ and $Sn(Zr_{0.5}Ti_{0.5})O_3$ have so far eluded attempts by many laboratories worldwide.[5]

Precious few Sn(II)-containing oxides have been synthesized as compared to other metal oxide systems. A primary reason is that as a reactant SnO is easily oxidized in air and disproportionates when heated under vacuum or in an inert atmosphere beginning at ∼300 °C.[8,9] Recent synthetic studies have demonstrated that low-temperature ion exchange reactions with Sn(II) halides, e.g., SnF_2 and/or $SnCl_2$, can provide an effective synthetic approach. Flux reaction conditions involve the use of relatively low-melting salts, e.g., metal chlorides or sulfates, as an effective medium to react metal oxides.[10] Its use has enabled the preparation of a growing number of new compounds which exhibit limited stability or metastability such as Sn_2TiO_4[11,12] or in related systems such as $Cu_2Ta_4O_{11}$ and $Cu_2Nb_8O_{21}$.[13,14] The recent examples with Sn(II) cations include the first high-purity

Received: January 6, 2020
Revised: March 8, 2020
Published: March 10, 2020

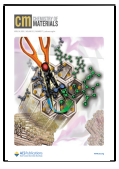

https://dx.doi.org/10.1021/acs.chemmater.0c00044
Chem. Mater. 2020, 32, 3054−3064

syntheses of Sn_2TiO_4, representing the first known Sn(II) titanate, as well as $SnTiO_3$ with an ilmenite structure type.[15] The former phase was synthesized starting from either $K_2Ti_2O_5$ or Ba_2TiO_4, e.g., $Ba_2TiO_4(s) + 2SnClF(s) \rightarrow Sn_2TiO_4(s) + 2BaClF(s)$. The exothermicity of salt formation drives the net reaction, with a large enthalpy of formation of BaClF from SnClF of about −1041 kJ mol^{-1}.[11] Thus, this approach leverages the exothermic formation of stable salts to surmount the thermodynamic barriers to forming metastable compounds.

Elucidation of the underlying chemistry that determines the synthesizability of metastable compounds currently represents a highly active research field. The fundamental principles and limits are not well understood and have historically remained primarily empirical in nature. One hypothesized criterion is that the synthesizability of a metastable compound can be determined based upon its excess enthalpy above the ground state, such as within a range of ∼0.05 to 0.20 eV $atom^{-1}$ above the convex hull in composition space. More recently, computational investigations have demonstrated that a greater cohesive energy enables the synthesis of compounds with a higher metastability.[16,17] Perovskite oxides represent a large family of compounds with relatively high cohesive energies that are a function of the A- and B-site cations.[18] A tuning of the mixed A/A′-site and B/B′-site cations in the form of solid solutions can be used as a chemical lever to manipulate their relative stability. Perovskite compounds can serve as a testbed for exploring the underlying principles of the synthesizability of metastable phases, such as for those containing Sn(II) cations. For example, the perovskite-type $SnTiO_3$ and $SnZrO_3$, as well as the $Sn(Zr_{0.5}Ti_{0.5})O_3$ solid solution, are all calculated to be highly metastable, by ∼0.4−0.5 eV $atom^{-1}$, with respect to decomposition to the simpler oxides or to the ilmenite structure. Prior studies have found that the largest amount of Sn(II) that can be incorporated into the A-site of any titanate or zirconate perovskite is limited to less than about 10 mol %.[19,20]

Described herein is the substitution of the destabilizing Sn(II) cation into the perovskite $BaZrO_3$, $BaTiO_3$, and the $Ba(Zr_{1-y}Ti_y)O_3$ solid solutions using low-temperature reactions with a salt flux and yielding highly metastable compositions. Perovskites are obtained in bulk form with the highest known amounts of Sn(II) cations and that push the extreme limits of metastability that can be synthesized. The compounds were comprehensively characterized and found to exhibit cubic perovskite structures that become increasingly metastable with both the Sn(II) and Zr(IV) concentrations. Their kinetic stabilization is attributable to the large cohesive energy of the underlying perovskite structure as well as the low reaction temperatures and short reaction time which mitigate ion diffusion and segregation. Their bandgaps and photocatalytic activities for water oxidation also show promising properties for solar energy conversion.

2. EXPERIMENTAL METHODS

2.1. Flux Synthesis of $Ba(Zr_{1-y}Ti_y)O_3$ Perovskites. The $BaTiO_3$, $BaZrO_3$, and $Ba(Zr_{1-y}Ti_y)O_3$ (BZT; y = 0.25, 0.5, 0.75) solid solutions were synthesized in a molten NaCl−KCl salt flux. The reactants $BaCO_3$ (0.0055 mol, Alfa Aesar, 99.8%), TiO_2 (0.0025 mol, J.T. Baker, >99%), and ZrO_2 (0.0025 mol, Beantown Chemical, 99.5%) were ground together for 20 min in the desired stoichiometry with a 10% mole excess of $BaCO_3$. After mixing, an equimolar mixture of NaCl (0.05 mol) and KCl (0.05 mol) was prepared with a salt-to-product ratio of 20:1 that was ground for 20 min. The reactants were loaded into an alumina crucible and heated to 1100 °C at a rate of 10 °C min^{-1} and soaked for 24 h before cooling to room temperature. Products were washed multiple times in deionized water and centrifuged to remove any salt flux and dried overnight at 80 °C.

2.2. Flux-Assisted Synthesis of $(Ba_{1-x}Sn_x)(Zr_{1-y}Ti_y)O_3$ (BSZT). The BSZT phases (y = 0.0, 0.25, 0.5, 0.75, 1.0; x = 0.1−1.0 in increments of 0.1) were synthesized via flux-assisted reactions using the $BaTiO_3$, $BaZrO_3$, BZT, and SnClF reactants. The perovskites (0.001 mol) were ground together with an appropriate stoichiometric amount of $SnCl_2$ (Alfa Aesar, 99% min) and SnF_2 (Alfa Aesar, 97.5%) under an argon atmosphere for 20 min and then loaded into a fused-silica tube and placed under a dynamic vacuum. The evacuated and flame-sealed tubes were then heated to 350 °C at a rate of 12 °C min^{-1}, held for 12 h, and radiatively cooled to room temperature. Products were thoroughly washed and centrifuged with deionized water to remove any unreacted salt flux or side products and dried overnight at 80 °C.

2.3. Characterization. Powder diffractograms for all samples were collected with a Rigaku R-Axis Spider using Cu Kα radiation (λ = 1.54056 Å) from a sealed tube X-ray source (40 kV, 36 mA) and a curved image-plate detector. High-resolution data sets for selected samples were collected on a PANalytical Empyrean X-ray diffractometer operating with Cu Kα radiation (45 kV, 40 mA) with a step size of 0.0131 2θ and a 300 s count time per step. X-ray total scattering measurements for reduced pair distribution function (PDF) analyses were collected at the 11-ID-C Beamline of the Advanced Photon Source (APS) at Argonne National Laboratory. A wavelength of 0.1173 Å was used for 2D data collection acquired using a PerkinElmer area detector. The reduction of the 2D data to 1D was performed by using FIT2d software. The PDF data were obtained from the 1D data by using PDFgetx3 software. Neutron diffraction data were collected on the POWGEN (Beamline 11-A) time-of-flight (TOF) diffractometer at the Spallation Neutron Source (SNS) at Oak Ridge National Laboratory during cycle run 2019-B. Polycrystalline samples (∼2 g) were sealed in cylindrical vanadium sample cans, and data were collected at 298 and 20 K. A neutron beam with a wavelength of 1.5 Å at 60 Hz was used with a detector ∼2.0−4.7 m away from the sample. The crystal structures were refined for both the X-ray and neutron diffraction data by the Rietveld method.

UV−vis diffuse reflectance measurements were taken by using a Shimadzu UV-3600 equipped with an integrating sphere. The background was a pressed barium sulfate disc. The data were transformed by using the Kubelka−Munk, $F(R)$, function.[21] Because $F(R)$ is also equal to k/s, where k and s are the absorption and scattering coefficients, the bandgaps can be extracted via Tauc plots of $(F(R) \times h\nu)^n$ versus photon energy for the allowed direct (n = 2) and indirect (n = 1/2) transitions. The direct and indirect bandgap energies were determined by extrapolating the linear portion of the Tauc plots to the baseline fit. SEM images and elemental analysis were performed by using a JEOL SM 6010LA scanning electron microscope with a 20 kV accelerating voltage with a secondary electron imaging detector along with a JEOL EDS silicon drift detector.

2.4. Suspended Particle Photocatalysis Measurements. Photocatalytic rates for molecular oxygen were measured without the addition of a cocatalyst by using similar conditions as reported previously.[22,23] The photocatalytic rates of molecular oxygen production were measured by using an outer-irradiation-type fused-silica reaction cell with a Xe arc lamp and photon flux of ∼200 mW cm^{-2}. The Xe arc lamp was equipped with an IR filter, and samples were irradiated with ultraviolet−visible light (λ > 230 nm) and visible light (λ > 400 nm). Suspensions were degassed via sonication with flowing nitrogen. Photocatalytic rates were measured in an aqueous 0.05 M $AgNO_3$ solution (Alfa Aesar, 99.9%). Measurements were taken every 10 min for 90 min to obtain the initial rate and then every 30 min thereafter. Gas production was measured volumetrically, and the products were identified via gas chromatography.

2.5. Electronic Structure Calculations. Total energy and electronic structure calculations were performed with 4 × 4 × 4

https://dx.doi.org/10.1021/acs.chemmater.0c00044
Chem. Mater. 2020, 32, 3054−3064

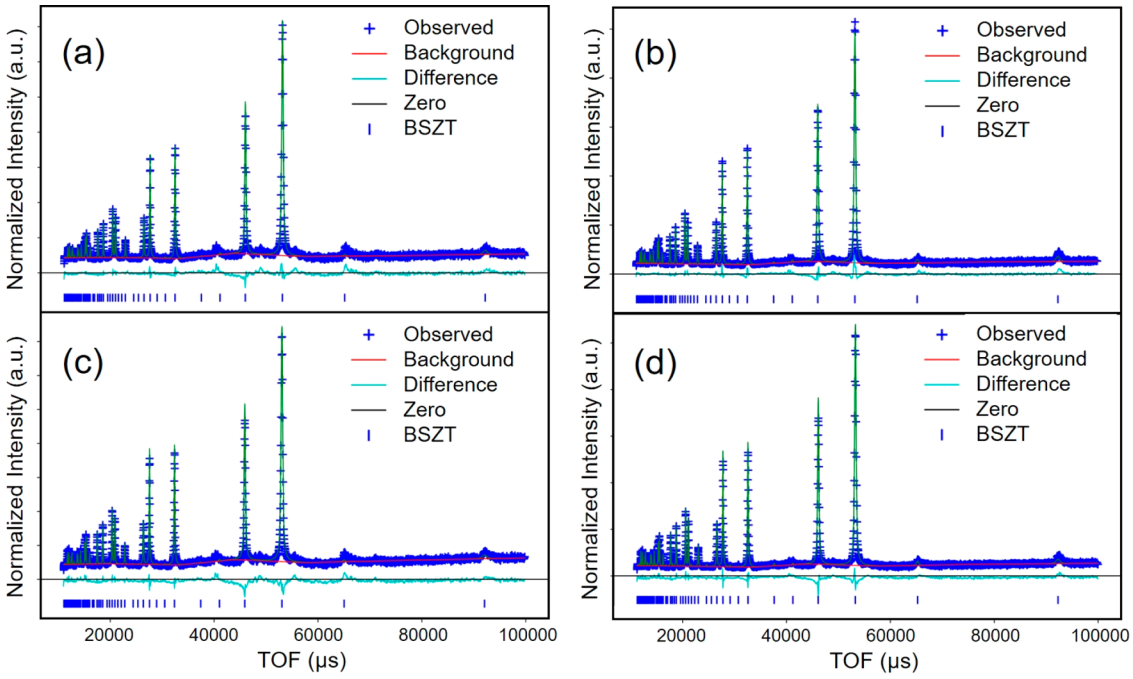

Figure 1. Plots of Rietveld refinements of neutron diffraction data at room temperature for (a) $(Ba_{0.6}Sn_{0.4})(Zr_{0.5}Ti_{0.5})O_3$ and (b) $(Ba_{0.4}Sn_{0.6})(Zr_{0.5}Ti_{0.5})O_3$ and at 20 K for (c) $(Ba_{0.6}Sn_{0.4})(Zr_{0.5}Ti_{0.5})O_3$ and (d) $(Ba_{0.4}Sn_{0.6})(Zr_{0.5}Ti_{0.5})O_3$ at 20 K.

supercells of $(Ba_{1-x}Sn_x)(Zr_{1-y}Ti_y)O_3$ using density functional theory methods as implemented in the Vienna Ab initio Simulation Package (ver. 4.6).[24,25] Calculations were performed using Perdew–Burke–Ernzerhof functionals in the generalized gradient approximation using the projector augmented wave method. The Brillouin zone was automatically sampled by using a 2 × 2 × 2 Monkhorst–Pack grid. The cubic phases of BZT and BSZT were simulated by using the cubic perovskite *Pm*-3*m* space group with lattice constants determined from the experimental values.

Decomposition energies of the Sn(II)-containing BSZT perovskites were calculated by following a previously reported procedure by Hautier et al.,[26,31] wherein the use of total energy calculations have been demonstrated to accurately predict reaction energies of ternary metal oxides from their binary oxides. Total energies are calculated at 0 K by using density-functional theory methods and then used to accurately calculate the overall reaction energy. As all reactants and products are solids, entropic contributions are assumed negligible at room temperature. For example, the decomposition of the Sn(II)-free oxides to their constituent binary oxides, i.e., $Ba(Zr_{1-y}Ti_y)O_3 \rightarrow BaO + (1 - y)ZrO_2 + yTiO_2$, were calculated to be thermodynamically unfavorable (ΔE_{decomp} of up to ~0.3 eV atom^{-1}). The reaction energy of decomposition of the metastable Sn(II)-containing perovskites was calculated according to the observed decomposition products, as described below. In nearly all cases the Sn(II)-containing perovskites decomposed via the formation of SnO and stoichiometric amounts of $Ba(Zr_{1-y}Ti_y)O_3$, TiO_2, and ZrO_2. Total energies of the binary oxides and the specific BZT/BSZT compositions were calculated as well as taken or cross-checked with the Open Quantum Materials Database.[27]

3. RESULTS AND DISCUSSION

3.1. Synthesis and Structural Characterization. Low-temperature flux-assisted reactions were investigated to prepare Sn(II)-containing perovskites starting from the barium perovskites, i.e., $Ba(Zr_{1-y}Ti_y)O_3 + xSnClF \rightarrow (Ba_{1-x}Sn_x)(Zr_{1-y}Ti_y)O_3 + xBaClF$. While pure $BaTiO_3$ is tetragonal, all other BZT compositions in this study (i.e., ≥25% Zr, $y = 0.75$) crystallize in the cubic polymorph at room temperature. The $Ba(Zr_{1-y}Ti_y)O_3$ compositions were reacted with SnClF to produce $(Ba_{1-x}Sn_x)(Zr_{1-y}Ti_y)O_3$ (BSZT) in increasing increments of 0.1 ($x = 0.0–1.0$). Bulk powder XRD data for each composition are shown in Figures S1–S5. Representative powder XRD data of unwashed BSZT show the formation of increasing amounts of BaClF, shown in Figure S6. The highest percentage of Sn(II) substitution into $BaTiO_3$, i.e., $(Ba_{1-x}Sn_x)TiO_3$, that maintained the perovskite structure was only ~10%, or $x = 0.1$. Higher amounts of Sn(II) substitution resulted in the formation of the ilmenite-type $SnTiO_3$ in increasing amounts. With a small increase of 25% Zr on the B-site, i.e., $Ba(Zr_{0.25}Ti_{0.75})O_3$, closer to ~40% Sn(II) could be substituted before the formation of the ilmenite-type $SnTiO_3$ phase. Starting from pure $BaZrO_3$, the maximum amount of Sn(II) substitution in $(Ba_{1-x}Sn_x)ZrO_3$ is further significantly increased to ~50% to 60%, or $x = 0.5–0.6$. This represents the highest Sn(II) concentration ever reported on the A-site for a perovskite-type structure. No evidence is found for an ilmenite-type "$SnZrO_3$" composition at higher amounts. Instead, higher amounts of Sn(II) in the loaded reaction stoichiometry result in increasing diffraction peaks for a SnO impurity.

A high amount of Sn(II) substitution was also possible in the 50:50 $BaZrO_3$–$BaTiO_3$ solid solution, i.e., $Ba(Zr_{0.5}Ti_{0.5})O_3$, with up to ~60% Sn(II) cations and the maintenance of the cubic perovskite structure. The powder XRD data show a minor amount of ZrO_2 impurity in all samples beyond ~30% Sn(II) concentration. However, the EDS data of the washed samples, listed in Table S1, show that up to ~60% Sn(II) can be incorporated into the structure. The compositional trends in the EDS data are also consistent with the loaded stoichiometries of each reaction, within a standard deviation of ~5%. To probe these structures in more detail, high-resolution X-ray diffraction data were collected for $Ba(Zr_{0.5}Ti_{0.5})O_3$ and for its compositions with 20%, 40%, and 60% Sn(II) cations to perform Rietveld refinements (Figure S7). High-resolution neutron diffraction data were also collected for the latter two compositions for Rietveld analyses

https://dx.doi.org/10.1021/acs.chemmater.0c00044
Chem. Mater. 2020, 32, 3054–3064

Table 1. Results of Rietveld Refinements of Neutron and X-ray Diffraction Data at Room Temperature for Selected Compositions of the $(Ba_{1-x}Sn_x)(Zr_{0.5}Ti_{0.5})O_3$ Solid Solution

loaded composition	$BaZr_{0.5}Ti_{0.5}O_3$ (0% Sn)	$Ba_{0.8}Sn_{0.2}Zr_{0.5}Ti_{0.5}O_3$ (20% Sn)	$Ba_{0.6}Sn_{0.4}Zr_{0.5}Ti_{0.5}O_3$ (40% Sn)		$Ba_{0.4}Sn_{0.6}Zr_{0.5}Ti_{0.5}O_3$ (60% Sn)	
radiation	X-ray	X-ray	X-ray	neutron	X-ray	neutron
lattice constant [Å]	4.095(1)	4.097(0)	4.095(9)	4.0922(8)	4.093(7)	4.090(8)
$R(w)$ [%]	4.67	3.55	3.25	5.69	3.67	5.90
Ba fraction	1.0[a]	0.82(3)	0.61(9)	0.58(8)	0.400[a]	0.400[a]
Sn fraction	0.0[a]	0.17(7)	0.38(1)	0.41(2)	0.600[a]	0.600[a]
Zr fraction	0.47(3)	0.44(5)	0.47(7)	0.45(1)	0.47(0)	0.48(5)
Ti fraction	0.52(7)	0.55(5)	0.52(3)	0.54(9)	0.53(0)	0.51(5)

[a]Value was fixed during refinement.

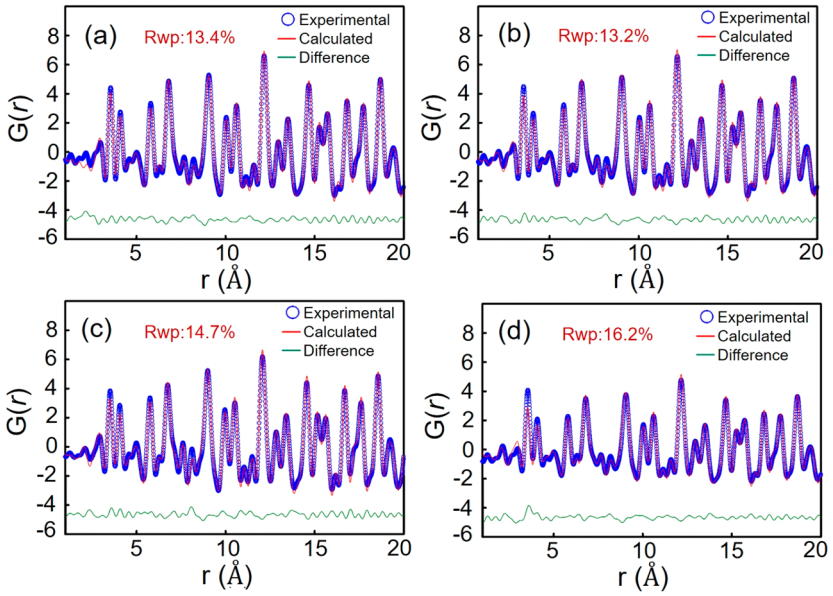

Figure 2. Pair distribution function refinements for (a) $Ba(Zr_{0.5}Ti_{0.5})O_3$, (b) $(Ba_{0.8}Sn_{0.2})(Zr_{0.5}Ti_{0.5})O_3$, (c) $(Ba_{0.8}Sn_{0.2})(Zr_{0.25}Ti_{0.75})O_3$, and (d) $(Ba_{0.4}Sn_{0.6})(Zr_{0.5}Ti_{0.5})O_3$. The cubic perovskite model was used for refinements.

(Figure 1). Results of the Rietveld refinements of the $(Ba_{1-x}Sn_x)(Zr_{0.5}Ti_{0.5})O_3$ compositions (Table 1) most closely matched with a cubic perovskite structure, with weighted residuals of ~3−6%.

The lattice constant was found to slightly contract with Sn(II) substitution and ranged from 4.095(1) to 4.090(8) Å. In addition, the refined elemental distributions of Ba/Sn cations on the A-site and the Zr/Ti cations on the B-site were consistent with the loaded reaction stoichiometries. Neutron diffraction data were also taken at 20 K for the 40% and 60% Sn(II) perovskites to probe whether a low-temperature phase transition occurs, similar to that known for $BaTiO_3$ and the $Ba(Zr_{1-y}Ti_y)O_3$ solid solution. Both compositions remained well matched to the cubic perovskite structure at low temperatures (Figure 1c,d and Table S2), with only a small contraction of the lattice constant.

The BSZT compositions all surprisingly indicated the lack of a stereoactive lone pair on the Sn(II) cation. The Sn(II) cation is predicted to undergo an atomic displacement similar to the isoelectronic Pb(II) cation in the well-known PZT compositions. All previously reported crystal structures of binary and ternary Sn(II)-containing oxides have shown the presence of a stereoactive lone pair. To investigate the local structures, total X-ray scattering data were collected, and the pair distribution functions (PDFs) were calculated for representative compositions.[28,29] These data are shown in Figure 2 for $Ba(Zr_{0.5}Ti_{0.5})O_3$ with 0%, 20%, and 60% Sn(II) substitution and for $Ba(Zr_{0.25}Ti_{0.75})O_3$ with 20% Sn(II) substitution. The refinement results confirmed the long-range structures and contracting unit cell dimensions of these cubic perovskite structures. In Figure S9 the calculated PDF's at small distances (r < 8.0 Å) show that all interatomic distances are consistent with the cubic perovskite model. However, the local structure (r < 3.0 Å) for the 60% Sn(II) perovskite indicated some small deviations from the ideal cubic symmetry (Figure 2d), which has so far not been adequately modeled in the refinements as it requires more model complexity. Preliminary results show that the introduction of a pseudocubic structure, which allows for small distortions to be modeled in the Sn(II) position along the [001] and [111] directions, may likely improve the Rietveld refinement results for the 60% Sn composition when compared with the cubic lattice structure. However, these refinements exhibit instabilities and necessitate further ongoing investigations and deeper analyses.

The stereoactivity of the post-transition-metal oxides has been explained by the revised lone pair model (RLP) previously.[30] In brief, metal cations with electron configurations $d^{10}s^2p^0$ in groups 13−16 can exhibit stereoactive lone pairs arising from the mixing of the unoccupied cation p orbitals with the antibonding cation s and anion p states. Strong lone-pair activity occurs when the cation s and anion p states are close in energy, such as for Sn(II) cations bonded to

https://dx.doi.org/10.1021/acs.chemmater.0c00044
Chem. Mater. 2020, 32, 3054−3064

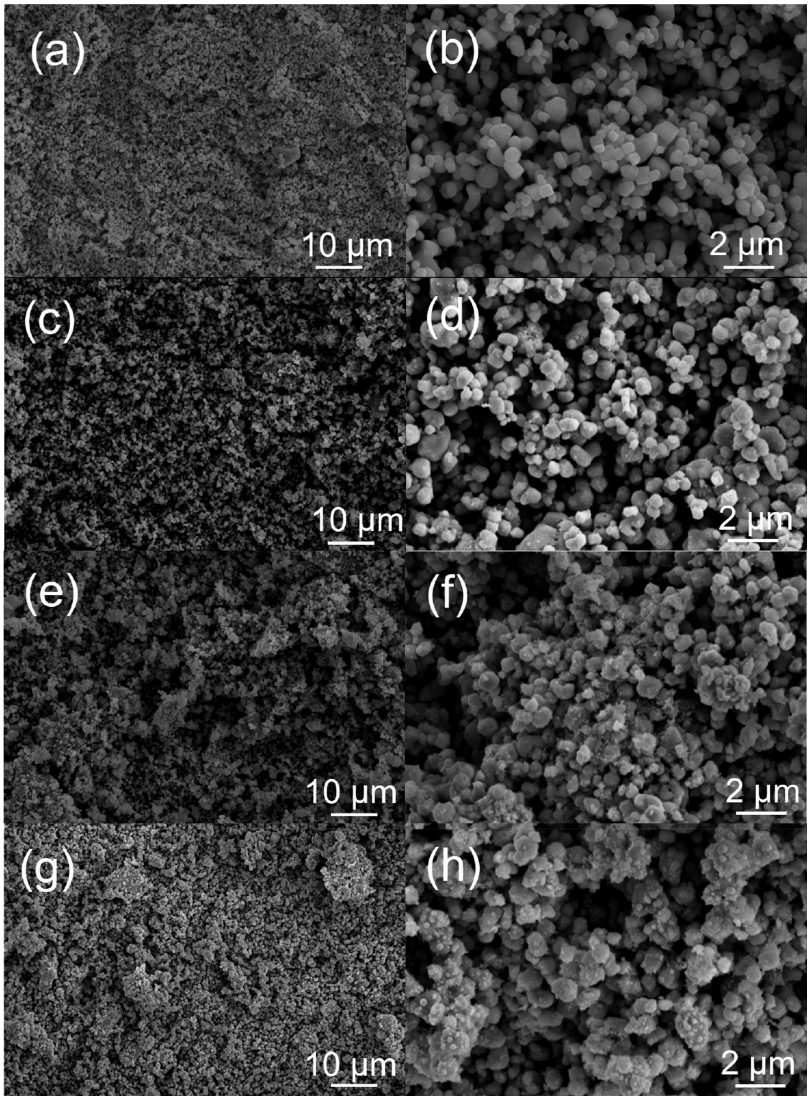

Figure 3. SEM images of (a, b) $Ba(Zr_{0.5}Ti_{0.5})O_3$, (c, d) $(Ba_{0.8}Sn_{0.2})(Zr_{0.5}Ti_{0.5})O_3$, (e, f) $(Ba_{0.6}Sn_{0.4})(Zr_{0.5}Ti_{0.5})O_3$, and (g, h) $(Ba_{0.4}Sn_{0.6})(Zr_{0.5}Ti_{0.5})O_3$. Particle sizes ranged ~0.5 to 2.0 μm.

oxygen. Additionally, the net electronic stabilization must be greater than the energetic penalty from the decrease in coordination. Based on the RLP model, the lack of lone pair activity appears unusual. However, the mixed A/A′-site of BSZT contains both Ba(II) and Sn(II), of which only the latter has the requisite electronic configuration to favor a structural distortion. A greater Sn(II) substitution on the A-site would lead to a larger concerted electronic driving force to give the distorted perovskite structure, as predicted for $SnTiO_3$ or $Sn(Zr_{0.5}Ti_{0.5})O_3$. The lack of a lone pair is thus attributed to the energetic penalty for the decrease in coordination of both Ba(II) and Sn(II) being greater than the electronic stabilization afforded to Sn(II) in a distorted environment.

3.2. Particle Sizes and Morphologies. Scanning electron microscope (SEM) images were taken to measure the particle sizes and morphologies of the perovskite products both before and after the substitution of the Sn(II) cations. This was used to probe for evidence of whether the perovskite structure had melted and recrystallized or, alternatively, if a relatively "soft" Sn(II) exchange had occurred to give the products without it melting. Shown in Figure 3 are the SEM images taken for the $(Ba_{1-x}Sn_x)(Zr_{0.5}Ti_{0.5})O_3$ family of compounds, for 0%, 20%, 40%, and 60% Sn(II) substitution. The crystallite particles of the unsubstituted $Ba(Zr_{0.5}Ti_{0.5})O_3$ (Figure 3a,b) exhibited an almost cubic-shaped morphology with smooth surfaces and sizes ranging from ~0.5 to 2 μm. The perovskite with 20% Sn(II) substitution (Figure 3c,d) showed the same general particle sizes but with slightly more irregular morphologies with roughened surfaces. The perovskite samples with 40% and 60% Sn(II) substitution showed the same trend.

Significantly, no evidence was found for particle coarsening or agglomerating that would indicate the melting or dissolution of the $Ba(Zr_{0.5}Ti_{0.5})O_3$ particles during the substitution of the Sn(II) cations. The incorporation of Sn(II) cations can even be achieved to some extent without the breakup of the particles, up to about 20% Sn(II). However, the addition of larger amounts of Sn(II) significantly fractures the particles because of the difference in ionic size between the Ba(II) and Sn(II) cations, which have crystal radii of ~1.35 and ~0.95 Å, respectively. As the crystal radius of 12-fold coordinate Sn(II) is unknown, the preceding values for 6-fold coordination are used only as a common reference point to compare the relative crystal radii of Ba(II) and Sn(II). The trends in the measured Ba:Sn molar ratios from energy dispersive X-ray spectroscopy

https://dx.doi.org/10.1021/acs.chemmater.0c00044
Chem. Mater. 2020, 32, 3054−3064

were consistent with the results of the structure refinements and the loaded reaction stoichiometries (Table S1).

3.3. Thermodynamic Calculations of Stability. To probe the stability of the perovskite oxides, total energies of each of the compositions were obtained from DFT results available in the Open Quantum Materials Database. Some solid solutions were also calculated for consistency using the VASP software package. Prior studies by Hautier et al. have demonstrated that total energies can be used to determine the reaction energies for the formation of metal oxides at 0 K.[31] The calculated reaction energies have been shown to be accurate within a mean deviation of close to zero and a standard deviation of only ~24 meV atom^{-1}, i.e., much smaller than the reaction energies. The reaction energies, e.g., AO + BO_2 → ABO_3, indicate the extent of metastability (ΔE_{decomp} > 0) of the perovskite toward decomposition to a more stable polymorph or the binary oxides. Stabilities were estimated as a function of both A/A′- and B/B′-site compositions.

The decomposition pathways calculated for the $(Ba_{1-x}Sn_x)$-$(Zr_{1-y}Ti_y)O_3$ (BSZT) perovskites were based upon the experimentally observed products at each composition. For example, both of the pure Sn(II)-based perovskites are highly thermodynamically unstable with respect to decomposition to the binary oxides, e.g., $SnZrO_3$ → SnO + ZrO_2 by a significant ~2.3 eV formula^{-1} (~0.46 eV atom^{-1}). By comparison, $BaZrO_3$ is thermodynamically stable with respect to decomposition to the constituent binary oxides. For a mixed Ba(II)/Sn(II) solid solution the decomposition is calculated according to the following reaction: $2(Ba_{0.5}Sn_{0.5})ZrO_3$ → $BaZrO_3$ + SnO + ZrO_2. The decomposition products are consistent with the experimental product distributions, as shown for example in Figures S10 and S11. In a mixed Ba(II)/Sn(II) and Ti(IV)/Zr(IV) solid solution of BSZT, the decomposition reaction proceeds by the formation of a mixture of SnO and ZrO_2/TiO_2.

The decomposition energies of the reactions were calculated and are plotted in Figure 4 as a function of the A/A′-site (Ba/Sn; *x*-axis) and B/B′-site (Zr/Ti; *y*-axis) compositions in the $BaTiO_3$–$BaZrO_3$–$SnTiO_3$–$SnZrO_3$ system. All 100% Sn(II)-based perovskites are thermodynamically unstable; e.g., $SnTiO_3$ is thermodynamically unstable with respect to decomposition to SnO and TiO_2 by a significant ~2.0 eV formula^{-1} (~0.40 eV atom^{-1}). Starting from the thermodynamically stable $BaTiO_3$, an increasing substitution of Sn(II) into the structure can be modeled as the solid solution $(Ba_{1-x}Sn_x)TiO_3$ with increasing *x*, shown in Figure 4 (upper right *x*-axis). The solid solution rapidly becomes unstable with respect to decomposition beyond $x \sim 0.15$ or ~15% Sn(II) cations, in agreement with prior synthetic studies using high-temperature conditions that have found ~10% or less of Sn(II) can be incorporated into titanate perovskites. Similar results are found for the zirconate analogue, i.e., $(Ba_{1-x}Sn_x)ZrO_3$ in Figure 4 (*x*-axis; lower left), which is predicted to be metastable beyond ~15% Sn(II) cations. Consistent results are found for Sn(II) substitution across the entire mixed-Ti/Zr composition range of the $(Ba_{1-x}Sn_x)(Zr_{1-y}Ti_y)O_3$ solid solution. At all compositions, a higher Sn(II) content leads to a rapid decrease in stability with a nearly linear negative slope in the perovskite formation energy of ~0.5 eV formula^{-1}.

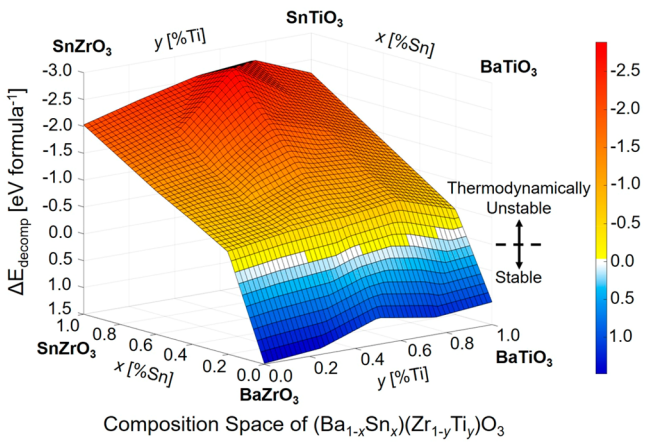

Figure 4. Calculated reaction energy landscape for perovskite decomposition at 0 K in the composition space spanning $BaTiO_3$–$BaZrO_3$–$SnTiO_3$–$SnZrO_3$, as representing the mixed A/A′- and B/B′-site solid solution $Ba_{1-x}Sn_xZr_{1-y}Ti_yO_3$. The orange to red colors denote increasing instability, and the light blue to dark blue colors indicate increasing stability.

An enhanced synthesizability of metastable perovskites containing Sn(II) cations is found with an increasing Zr substitution on the B-site, although these compositions are more highly metastable. With 0% Zr, i.e., $BaTiO_3$, only ~10% Sn(II) could be substituted before the product converted to the more stable ilmenite structure type. However, up to 50%–60% Sn(II) substitution could be achieved in the perovskite structure when Zr(IV) cations were substituted for Ti(IV) cations on the B-site, leading to the metastable $(Ba_{0.5}Sn_{0.5})$-ZrO_3 or $(Ba_{0.4}Sn_{0.6})(Ti_{0.5}Zr_{0.5})O_3$. These compositions occur in the areas of high metastability (Figure 4) and are highly unstable with respect to decomposition to the binary oxides by ~0.27 and ~0.25 eV atom^{-1}, respectively. By comparison, it has typically been considered that an excess free energy above some empirically defined limit, e.g., ranging from ~0.05 to 0.15 eV atom^{-1}, will render a metastable phase not synthesizable.[16,17] The Sn(II)-substitution obtained by the low-temperature flux reactions greatly exceeds the thermodynamic limits of stability with a metastability that has not been found by using high-temperature synthetic methods.

Possible explanations for the successful synthesis of the highly metastable BSZT compositions are the configurational entropy and/or the kinetic stabilization provided by the high cohesive energy of the underlying perovskite network. As has been shown for entropy-stabilized oxides and alloys, enhanced phase stability can result when a large number of different elements are mixed and disordered over the same crystallographic sites.[32,33] For BSZT, which has two sites mixed with two metal cations, the calculated S_{max} is only on the order of ~5.0×10^{-5} eV K^{-1} or ~0.015 eV at room temperature. This is significantly smaller than the calculated decomposition energies, showing this is too small to be responsible for the stabilization of BSZT. Furthermore, entropy stabilized solids become more stable with increasing temperature rather than decompose as observed for BSZT. While the $(Ba_{0.7}Sn_{0.3})$-$(Zr_{0.5}Ti_{0.5})O_3$ composition can be successfully synthesized, exchange reactions performed at higher temperatures for longer time clearly result in decomposition (Figure S10). Additionally, heating of the BSZT compositions with >10% Sn(II) cations at higher temperatures leads to decomposition (Figure S11).

Large-scale studies have shown that metastable phases are more frequently found, i.e., synthesizable, when they have higher cohesive energies.[16,17] These findings lead to the

https://dx.doi.org/10.1021/acs.chemmater.0c00044
Chem. Mater. 2020, 32, 3054–3064

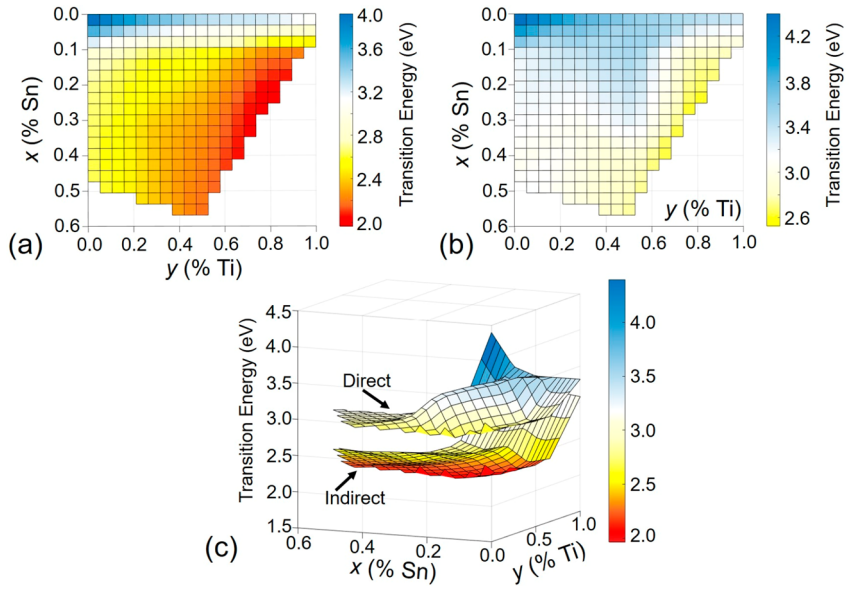

Figure 5. Experimentally observed indirect bandgap size (a) and direct bandgap transition (b) of $(Ba_{1-x}Sn_x)(Zr_{1-y}Ti_y)O_3$ as a function of the Ba/Sn A-site (x-axis) and Zr/Ti B-site (y-axis) compositions. Both the direct and indirect bandgap transitions are plotted together in (c). The blue to yellow to red colors indicate the decreasing bandgap sizes.

intuitive idea that stronger bonds are more capable of "locking in" energetically unfavorable atomic arrangements. Furthermore, the likelihood of a ground state of a metastable phase being phase separated rather than polymorphic increases with the number of elements, with inhibition of the atomic diffusion and segregation providing a kinetic barrier for decomposition to more thermodynamically favored products.[16] Perovskite oxides have been found to exhibit relatively high cohesive energies, especially for zirconates,[18] and can therefore kinetically stabilize against decomposition by inhibiting significant cation and anion diffusion. The above factors help to understand the high amount of Sn(II) that can be substituted under these reaction conditions into different compositions of the $Ba(Zr_{1-y}Ti_y)O_3$ perovskite. The synthesis of metastable $(Ba_{1-x}Sn_x)(Zr_{1-y}Ti_y)O_3$ (BSZT), with a positive free energy of formation, is driven by the larger negative free energy of formation of BaClF in the reaction. The low reaction temperature, short reaction time, and high cohesive energy of the BZT phases inhibit long-range ion diffusion. When comparing $BaTiO_3$ and $BaZrO_3$, the former readily converts to the ilmenite structure type with the substitution of >10% Sn(II) cations of the same composition without the need for significant ion diffusion. By contrast, the ilmenite structure is not stable for the zirconate perovskite and must therefore decompose by significant cation diffusion and segregation into simpler binary oxides. As compared to $BaTiO_3$, the $BaZrO_3$ perovskite also has a higher cohesive energy (−41.43 eV vs −39.69 eV) and a significantly higher melting point (2700 °C vs 1625 °C). As a result, $BaZrO_3$ can incorporate a much higher amount of ∼50−60% Sn(II) cations with a high metastability before the onset of decomposition.

A high metastability is also achieved for the mixed B-site solid solution of 50% Zr(IV) and 50% Ti(IV) cations, i.e., starting from the $Ba(Zr_{0.5}Ti_{0.5})O_3$ perovskite. In this perovskite up to ∼60% Sn(II) can be attained, i.e., $(Ba_{0.4}Sn_{0.6})(Zr_{0.5}Ti_{0.5})O_3$. Its decomposition is inhibited as significant ion diffusion is required for decomposition to occur to give the binary oxides ZrO_2 and SnO. The $Ba(Zr_{0.5}Ti_{0.5})O_3$ solid solution is the composition where both the Zr(IV) and Ti(IV) are the most diluted in the perovskite lattice, and consequently, the greatest ion diffusion is required for decomposition. For example, the synthesis of MS_2 (M = Fe, Co, and Ni) has similarly shown that crystalline metastable intermediates are observed during the reaction of Na_2S_2 with MCl_2 that are trapped because of the limited ion diffusion achieved under low-temperature solid-state reaction conditions in a similar fashion to BSZT.[34] This suggests that an effective approach for the synthesis of metastable phases is the dilution of multiple different cations over equivalent crystallographic sites, requiring maximal ion diffusion for their decomposition.

3.4. Optical Properties and Electronic Structure. Metal oxides containing the Sn(II) cation are under intense investigation as small bandgap semiconductors. Optical absorption measurements were taken to probe how the increasing Sn(II) substitution impacts the bandgap. The direct and indirect bandgap energies are plotted together in Figure 5 as a function of the mixed A/A′-site (Ba/Sn; x-axis) and B/B′-site (Zr/Ti; y-axis) stoichiometries. All compositions show a lowest energy indirect bandgap transition spanning a wide range from ∼3.90 eV for $BaZrO_3$ to ∼1.95 eV for $(Ba_{0.7}Sn_{0.3})(Zr_{0.25}Ti_{0.75})O_3$, with direct bandgaps for each composition that is ∼0.2−0.8 eV higher in energy. The bandgap is generally found to decrease with increasing Sn(II) and Ti(IV) compositions, as labeled by the red areas in Figure 5a. As the Sn(II) concentration increases, an absorption edge at lower energy forms and grows as a result of the increasing density of the Sn(II) states in the valence band. These results are consistent with prior research on solid solutions with tunable chemical compositions.[35,36] Compositions with the largest amounts of Sn(II) cations exhibit the smallest bandgaps, e.g., 1.95 eV for $(Ba_{0.7}Sn_{0.3})(Zr_{0.25}Ti_{0.75})O_3$, 2.14 eV for $(Ba_{0.4}Sn_{0.6})(Zr_{0.5}Ti_{0.5})O_3$, and 2.40 eV for $(Ba_{0.7}Sn_{0.3})(Zr_{0.75}Ti_{0.25})O_3$. The regions of the BSZT composition space with the smallest bandgaps also correspond to the areas of highest metastability in Figure 4. The ZrO_2 impurity found in some samples exhibits a bandgap of >5.0 eV, significantly

https://dx.doi.org/10.1021/acs.chemmater.0c00044
Chem. Mater. 2020, 32, 3054−3064

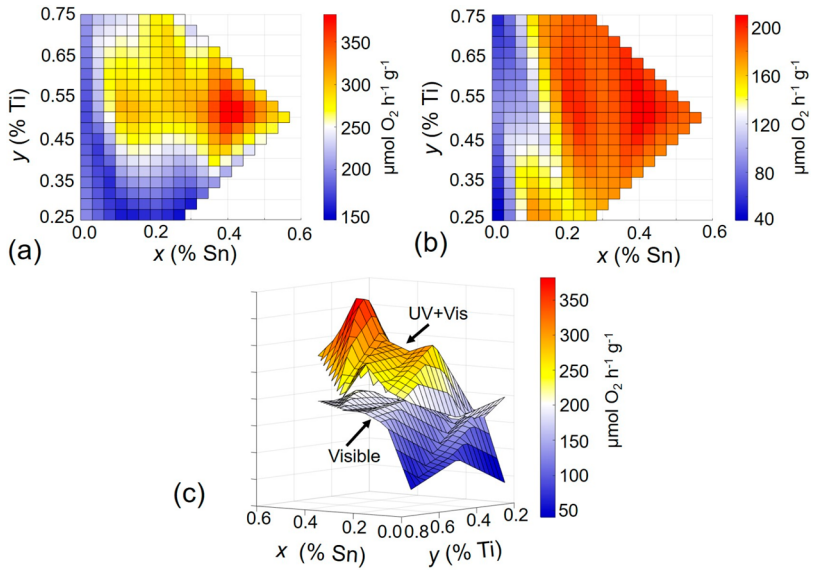

Figure 6. Plots of photocatalytic rates of suspended particles of $(Ba_{1-x}Sn_x)(Zr_{1-y}Ti_y)O_3$, as a function of the Ba/Sn A-site (x-axis) and Zr/Ti B-site (y-axis) compositions for molecular oxygen evolution (μmol O_2 h^{-1} g^{-1}) under combined ultraviolet + visible light (λ > 230 nm) (a) or under only visible-light irradiation (λ > 400 nm) (b). Both ultraviolet + visible and only visible light are plotted together in (c). The blue to red coloring denotes higher photocatalytic rates.

higher in energy than found for the BSZT phases. These results show an underlying relationship between high metastability and the formation of the smallest bandgaps.

The dependence of the bandgap on the BSZT composition can be fitted to the standard bowing equation:[37]

$$E_g^{BSZT}(x) = E_g^1 x + E_g^2(1-x) - bx(1-x)$$

where E_g^1 and E_g^2 are the bandgaps of the end point compositions, x is the mole fraction of each, and b is the bowing parameter. Starting from ~10% Sn(II) in each BSZT composition, an increasing Sn(II) substitution could be well-fitted to a bowing parameter of 0.45 eV. The largest change in the indirect bandgap occurred with the increase from 0% to 10% Sn(II) cations, decreasing the bandgap by a consistent ~0.75−0.9 eV for all compositions. For example, the 3.30 eV bandgap size of $Ba(Zr_{0.5}Ti_{0.5})O_3$ was decreased to 2.54 eV with the introduction of only 10% Sn(II) cations. The bowing parameter value, fitted from 10% to 60% Sn(II) cations, represents the extent of band widening and dispersion that occurs with increasing amounts of −O−Sn−O−Sn−O connectivity within the structure. The band dispersion also has a significant impact on the energetic separation between the indirect and direct bandgap transitions that increases with the Sn(II) and Ti(IV) cations, shown in Figure 5c, with the valence band widening having a predominant effect on the indirect transition.

Electronic structure calculations were performed to probe the origins of the changes in the bandgap with increasing Sn(II) substitution, given in Figure S14. For $Ba(Zr_{0.5}Ti_{0.5})O_3$, the bandgap is primarily set by the energetic distance between the Ti 3d- and O 2p-based states, with the Zr 4d orbitals located at higher energies. After substitution of 60% Sn(II) cations, the valence band is now composed of strongly interacting Sn 5s and O 2p states, with a shift of the valence band edge to higher energies. These results are consistent with prior electronic structure investigations of Sn(II)-containing oxides, wherein the Sn 5s orbitals interact with the O 2p orbitals at the valence band edge and result in a smaller bandgap.[1,11] As the concentration of Sn(II) increases, the Sn 5s contributions in the valence band increases. This is a result of the extended −O−Sn−O−Sn−O− network that is formed with greater Sn(II) substitution and which increases the Sn−O antibonding interactions.

3.5. Suspended Particle Photocatalysis. Prior experimental and computational studies have predicted that Sn(II)-containing oxides frequently have favorable band energetics for efficient photocatalysis under sunlight.[1,11,12,26,27,38] For example, previous photocatalytic measurements on Sn_2TiO_4, with a bandgap of only ~1.55 eV, showed high activity for molecular oxygen evolution with an apparent quantum yield of ~1.0% under 420 nm irradiation.[11,12] Extended −O−Sn−O−Sn−O connectivity can result in highly disperse valence bands, yielding low carrier effective masses and high carrier mobilities.[2]

Photocatalytic activities across the full range of synthesizable $(Ba_{1-x}Sn_x)(Zr_{1-y}Ti_y)O_3$ (BSZT) powders were measured for molecular oxygen evolution. These rates are plotted collectively in Figure 6 as a function of the mixed A-site Ba/Sn (x) and B-site Zr/Ti (y) compositions. Photocatalytic rates were taken under combined ultraviolet and visible (UV + Vis) light (λ > 230 nm) or under only visible-light (λ > 400 nm) irradiation (Figures 6a and 6b, respectively). Bandgap transitions of the BZT phases, i.e., $Ba(Zr_{1-y}Ti_y)O_3$, all occur in the ultraviolet energies of >3.2 eV. Accordingly, these perovskites all showed little to no activity under visible-light irradiation, but relatively high activity under UV + Vis light of ~170−210 μmol O_2 h^{-1} g^{-1}. In contrast, the substitution of >10% Sn(II) cations in the BSZT phases, i.e., $(Ba_{1-x}Sn_x)(Zr_{1-y}Ti_y)O_3$, resulted in visible-light bandgaps and significantly higher activities under both ultraviolet and visible-light irradiation. The higher rates are attributable in part to the absorption of a larger fraction of visible-light wavelengths. Under combined ultraviolet−visible or visible-only irradiation, the highest measured photocatalytic activities peaked at around the $(Ba_{0.6}Sn_{0.4})(Zr_{0.5}Ti_{0.5})O_3$ composition with rates of ~408 and ~216 μmol O_2 h^{-1} g^{-1}, respectively. Conservative

https://dx.doi.org/10.1021/acs.chemmater.0c00044
Chem. Mater. 2020, 32, 3054−3064

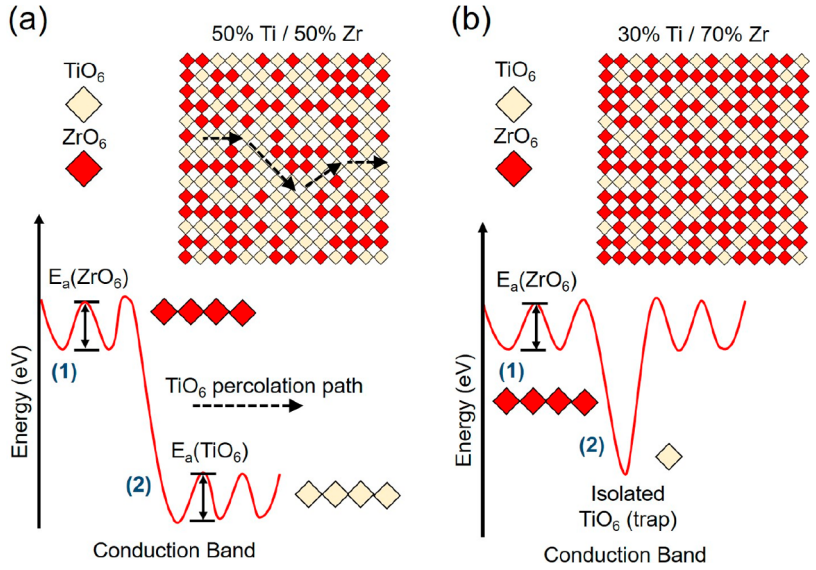

Figure 7. Schematic illustration of a TiO_6/ZrO_6 solid solution, red and white squares respectively, wherein the TiO_6 octahedra are mixed at a concentration below the percolation threshold (right) and above the percolation threshold (left). The energy diagrams (lower) show the polaron hopping with activation barriers (E_a) between the ZrO_6 or TiO_6 octahedra.

estimates of the apparent quantum yields (AQY) give lower limits of ~0.51% (230 nm < λ < 564 nm) and ~0.39% (400 nm < λ < 564 nm) for this composition. The bubbles of molecular oxygen that evolved very rapidly adhered strongly to the particles' surfaces, significantly slowing the apparent reaction rates that were measured volumetrically. This was a result of the particles becoming increasingly hydrophobic with increasing Sn(II) substitution.

The Sn(II)-containing BSZT compositions all showed similar high photocatalytic rates for molecular oxygen production under visible-light irradiation (Figure 6b), while there was a detectable peaking in the rates at x = 0.4 and y = 0.5 under combined ultraviolet−visible irradiation (Figure 6a). In this case the electrons are excited across the bandgap into a range of relatively lower to higher energies within the conduction band. As the conduction band is composed of a disordered distribution of the empty d-orbitals of the Ti(IV) and Zr(IV) cations, it might be assumed that a significant amount of local trapping of the excited electrons could predominate. Recent results have suggested that photocatalytic activities can peak beyond the percolation threshold of disordered solid solutions,[39] whereby extended diffusion pathways "open up" across the extended crystalline structure at specific compositions. The percolation threshold is defined by the concentration at which the charged carriers are no longer trapped in isolated, low-energy defects, but instead coalesce to form a new band with an accompanying delocalization of excited carriers.[40] An example of a two-dimensional percolation network is shown schematically in Figure 7 for a mixed TiO_6/ZrO_6 solid solution where the octahedra have 4-fold connectivity. The percolation pathways form the conduction band edge because of the lower energy Ti d-orbitals relative to the Zr d-orbitals. For a two-dimensional network the percolation threshold is reached at 50% Ti(IV) substitution, shown as white squares in Figure 7a, while it is not reached for only 30% Ti(IV) substitution (Figure 7b). For the former, the thermalization of the excited charge carriers to the band edges thus leads to delocalization throughout the percolation network, such as reported previously for the Nb(V)/Ta(V) cation solid solution.[39] Similarly, the holes will thermalize to the valence band edge composed of Sn-5s and O-2p based states and will become delocalized at Sn(II) concentrations that exceed the percolation threshold.

The percolation thresholds for both the A-site (Ba/Sn) and B-site (Ti/Zr) cations can be calculated to within a few percent for the three-dimensional cubic perovskite structure by using the equation by Shante and Kirkpatrick:[41]

$$z \times p_c = \frac{d}{d-1}$$

where z is the coordination number, p_c is the percolation threshold, and d is the lattice dimensionality. The percolation threshold is the minimum concentration of a cation to form a complete path of adjacent sites, i.e., −O−Ti−O−Ti−O− or −O−Sn−O−Sn−O−, extending to the particles' surfaces. For the A-site Sn(II) cations, with 12-fold coordination and a dimensionality of 3, the percolation threshold corresponds to a p_c(Sn) of only ~12.5%, and for the B-site Ti(IV) cations (z = 6, d = 3) this occurs at a p_c(Ti) of ~25%. Thus, all compositions with >12.5% Sn(II) cations have extended −O−Sn-O−Sn−O connectivity for diffusion pathways of the charge carriers to reach the surfaces. This Sn(II) concentration represents the threshold at which higher visible-light activity is observed across the entire range of BSZT compositions, as found in the red-shaded region in Figure 6b, consistent with the relationship between percolation theory, charge-carrier delocalization, and photocatalytic activity. For the conduction band states, all compositions with >25% Ti(IV) cations have extended −O−Ti−O−Ti−O connectivity to provide percolation pathways for excited electrons. This is consistent with the much lower ultraviolet−visible photocatalytic rates for all perovskites with 25% or less Ti(IV) cations, as found in the blue regions of Figure 6a. In this compositional region, the conduction electrons are more localized and have a higher probability for recombination rather than reaching the particles' surfaces to drive water oxidation. In the combined ultraviolet−visible photocatalytic data (Figure 6a), the peak in the highest photocatalytic rates is found for compositions with

https://dx.doi.org/10.1021/acs.chemmater.0c00044
Chem. Mater. 2020, 32, 3054−3064

~>25% Ti(IV) cations and >20% Sn(II) cations. This peak occurs under irradiation conditions where charge separation and diffusion have a major impact on photocatalytic rates, rather than simply a result of the smaller bandgaps.

It is notable that the photocatalytic rates and apparent quantum yields of the BSZT perovskites are comparable to those initially reported for what is currently the best oxygen-evolving photocatalyst, i.e., $BiVO_4$ of ~100 μmol O_2 h^{-1} g^{-1} and an AQY = 0.3%.[42] However, the bandgaps of the BSZT perovskites are smaller than $BiVO_4$ by about ~0.4−0.5 eV and can absorb a larger fraction of sunlight. By analogy, it should be strongly considered that further investigations into the optimal photocatalytic reaction conditions, including surface cocatalysts and film processing of the BSZT phases, will likely reveal much higher attainable rates and AQY's.

4. CONCLUSIONS

Flux-assisted reaction conditions were used to synthesize the highest known amounts of Sn(II) cations in a perovskite, $(Ba_{1-x}Sn_x)(Zr_{1-y}Ti_y)O_3$, consisting of mixed A-site Sn(II)/Ba(II) cations and B-site Ti(IV)/Zr(IV) cations in a statistically disordered distribution. The highest attainable Sn(II) substitutions were found for the Zr(IV)-richer compositions, of up to ~60% Sn(II) in $(Ba_{0.4}Sn_{0.6})(Zr_{0.5}Ti_{0.5})O_3$ or ~50−60% Sn(II) in $(Ba_{0.4}Sn_{0.6})ZrO_3$. These represented the most metastable perovskites that could be synthesized, with remarkably high reaction energies for decomposition of ~0.25−0.27 eV $atom^{-1}$. Their synthesizability is shown to be possible via the large cohesive energy of the underlying perovskite structure that limits the diffusion of ions required for decomposition to simpler oxides. The optical bandgaps decreased from ~3.90 to ~1.95 eV with higher Sn(II) and Ti(IV) compositions, in correlation with the compositions showing the highest metastability. The BSZT powders exhibited high photocatalytic rates under ultraviolet−visible or visible-light irradiation for molecular oxygen evolution that peaked at ~408 and ~216 μmol O_2 h^{-1} g^{-1}, respectively, for the $(Ba_{0.6}Sn_{0.4})(Zr_{0.5}Ti_{0.5})O_3$ composition. The highest rates were found for compositions that exceeded the percolation threshold for the A-site Sn(II) cations and the B-site Ti(IV) cations. These results demonstrate a new route to highly metastable perovskites to target their smaller optical bandgaps and favorable photocatalytic properties.

■ ASSOCIATED CONTENT

Supporting Information

The Supporting Information is available free of charge at https://pubs.acs.org/doi/10.1021/acs.chemmater.0c00044.

Additional experimental data are provided including powder X-ray diffractograms of washed and unwashed BSZT phases, decomposition products, Rietveld refinements of neutron and X-ray diffraction data, representative EDS spectra, PDF refinement results, UV−vis diffuse reflectance data as Tauc plots, photocatalytic rates for molecular oxygen evolution, and calculated densities-of-states plots (PDF)

■ AUTHOR INFORMATION

Corresponding Author

Paul A. Maggard − *Department of Chemistry, North Carolina State University, Raleigh, North Carolina 27695, United States;* orcid.org/0000-0002-3909-1590; Email: paul_maggard@ncsu.edu

Authors

Shaun O'Donnell − *Department of Chemistry, North Carolina State University, Raleigh, North Carolina 27695, United States*

Ching-Chang Chung − *Department of Materials Science and Engineering, North Carolina State University, Raleigh, North Carolina 27695, United States*

Abigail Carbone − *Department of Chemistry, North Carolina State University, Raleigh, North Carolina 27695, United States*

Rachel Broughton − *Department of Materials Science and Engineering, North Carolina State University, Raleigh, North Carolina 27695, United States*

Jacob L. Jones − *Department of Materials Science and Engineering, North Carolina State University, Raleigh, North Carolina 27695, United States*

Complete contact information is available at: https://pubs.acs.org/10.1021/acs.chemmater.0c00044

Notes

The authors declare no competing financial interest.

■ ACKNOWLEDGMENTS

A portion of this research used resources of the Advanced Photon Source, a U.S. Department of Energy (DOE) Office of Science User Facility operated for the DOE Office of Science by Argonne National Laboratory under Contract DE-AC02-06CH11357. A portion of these research efforts also used resources at the Spallation Neutron Source, a DOE Office of Science User Facility operated by the Oak Ridge National Laboratory. Additional components of this research were performed in part at the Analytical Instrumentation Facility (AIF) at North Carolina State University, which is supported by the State of North Carolina and the National Science Foundation (Award ECCS-1542015). The AIF is a member of the North Carolina Research Triangle Nanotechnology Network (RTNN), a site in the National Nanotechnology Coordinated Infrastructure (NNCI).

■ REFERENCES

(1) Noureldine, D.; Takanabe, K. State-of-the-Art Sn^{2+}-Based Ternary Oxides as Photocatalysts for Water Splitting: Electronic Structures and Optoelectronic Properties. *Catal. Sci. Technol.* **2016**, *6* (21), 7656−7670.

(2) Ha, V. A.; Ricci, F.; Rignanese, G. M.; Hautier, G. Structural Design Principles for Low Hole Effective Mass s-Orbital-Based p-Type Oxides. *J. Mater. Chem. C* **2017**, *5* (23), 5772−5779.

(3) Matar, S. F.; Baraille, I.; Subramanian, M. A. First Principles Studies of $SnTiO_3$ Perovskite as Potential Environmentally Benign Ferroelectric Material. *Chem. Phys.* **2009**, *355* (1), 43−49.

(4) Ribeiro, R. A. P.; de Lazaro, S. R. DFT/PBE0 Study on Structural, Electronic and Dielectric Properties of $SnZr_{0.5}Ti_{0.5}O_3$ Lead-Free Ferroelectric Material. *J. Alloys Compd.* **2017**, *714*, 553−559.

(5) Gardner, J.; Thakre, A.; Kumar, A.; Scott, J. Tin Titanate - the Hunt for a New Ferroelectric Perovskite. *Rep. Prog. Phys.* **2019**, *82*, 092501.

(6) Parker, W. D.; Rondinelli, J. M.; Nakhmanson, S. M. First-Principles Study of Misfit Strain-Stabilized Ferroelectric $SnTiO_3$. *Phys. Rev. B: Condens. Matter Mater. Phys.* **2011**, *84* (24), 1−7.

(7) Pitike, K. C.; Parker, W. D.; Louis, L.; Nakhmanson, S. M. First-Principles Studies of Lone-Pair-Induced Distortions in Epitaxial Phases of Perovskite $SnTiO_3$ and $PbTiO_3$. *Phys. Rev. B: Condens. Matter Mater. Phys.* **2015**, *91* (3), 1−8.

(8) Campo, C. M.; Rodríguez, J. E.; Ramírez, A. E. Thermal Behaviour of Romarchite Phase SnO in Different Atmospheres: A Hypothesis about the Phase Transformation. *Heliyon* **2016**, *2* (5), No. e00112.
(9) Gauzzi, F.; Verdini, B.; Maddalena, A.; Principi, G. X-Ray Diffraction and Mössbauer Analyses of SnO Disproportionation Products. *Inorg. Chim. Acta* **1985**, *104* (1), 1−7.
(10) Boltersdorf, J.; King, N.; Maggard, P. A. Flux-mediated Crystal Growth of Metal Oxides: Synthetic Tunability of Particle Morphologies, Sizes, and Surface Features for Photocatalysis Research. *CrystEngComm* **2015**, *17*, 2225−2241.
(11) O'Donnell, S.; Hamilton, A.; Maggard, P. A. Fast Flux Reaction Approach for the Preparation of Sn_2TiO_4: Tuning Particle Sizes and Photocatalytic Properties. *J. Electrochem. Soc.* **2019**, *166* (5), H3084−H3090.
(12) Boltersdorf, J.; Sullivan, I.; Shelton, T.; Wu, Z.; Gray, M.; Zoellner, B.; Osterloh, F.; Maggard, P. A. Flux Synthesis, Optical and Photocatalytic Properties of *n*-Type Sn_2TiO_4: Hydrogen and Oxygen Evolution Under Visible Light. *Chem. Mater.* **2016**, *28*, 8876−8889.
(13) King, N.; Sommer, R. D.; Watkins-Curry, P.; Chan, J. Y.; Maggard, P. A. Synthesis, Structure and Thermal Instability of the $Cu_2Ta_4O_{11}$ Phase. *Cryst. Growth Des.* **2015**, *15*, 552−558.
(14) Choi, J.; King, N.; Maggard, P. A. Metastable Cu(I)-Niobate Semiconductor with a Low-Temperature Nanoparticle-Mediated Synthesis. *ACS Nano* **2013**, *7* (2), 1699−1708.
(15) Diehl, L.; Bette, S.; Pielnhofer, F.; Betzler, S.; Moudrakovski, I.; Ozin, G. A.; Dinnebier, R.; Lotsch, B. V. Structure-Directing Lone Pairs: Synthesis and Structural Characterization of $SnTiO_3$. *Chem. Mater.* **2018**, *30* (24), 8932−8938.
(16) Sun, W.; Dacek, S. T.; Ong, S. P.; Hautier, G.; Jain, A.; Richards, W. D.; Gamst, A. C.; Persson, K. A.; Ceder, G. The Thermodynamic Scale of Inorganic Crystalline Metastability. *Sci. Adv.* **2016**, *2* (11), No. e1600225.
(17) Aykol, M.; Dwaraknath, S. S.; Sun, W.; Persson, K. A. Thermodynamic Limit for Synthesis of Metastable Inorganic Materials. *Sci. Adv.* **2018**, *4*, No. eaaq0148.
(18) Goudochnikov, P.; Bell, A. J. Correlations Between Transition Temperature, Tolerance Factor and Cohesive Energy in 2+:4+ Perovskites. *J. Phys.: Condens. Matter* **2007**, *19*, 176201.
(19) Suzuki, S.; Honda, A.; Iwaji, N.; Higai, S.; Ando, A.; Takagi, H.; Kasatani, H.; Deguchi, K. Ferroelectricity of Sn-Doped $SrTiO_3$ Perovskites with Tin at Both A and B Sites. *Phys. Rev. B: Condens. Matter Mater. Phys.* **2012**, *86* (6), 8−11.
(20) Suzuki, S.; Honda, A.; Suzuki, K.; Higai, S.; Ando, A.; Niwa, K.; Hasegawa, M. Effects of Sn^{2+} ion Size on Sn Doped $SrTiO_3$. *Jpn. J. Appl. Phys.* **2013**, *52*, 09KC04.
(21) Simmons, E. L. Reflectance Spectroscopy: Application of the Kubelka-Munk Theory to the Rates of Photoprocesses of Powders. *Appl. Opt.* **1976**, *15* (4), 951.
(22) Boltersdorf, J.; Wong, T.; Maggard, P. A. Synthesis and Optical Properties of Ag(I), Pb(II), and Bi(III) Tantalate-Based Photocatalysts. *ACS Catal.* **2013**, *3*, 2943−2953.
(23) McLamb, N.; Sahoo, P. P.; Fuoco, L.; Maggard, P. A. Flux Growth of Single-Crystal $Na_2Ta_4O_{11}$ Particles and their Photocatalytic Hydrogen Production. *Cryst. Growth Des.* **2013**, *13*, 2322−2326.
(24) Kresse, G.; Furthmuller. Efficiency of Ab-Initio Total Energy Calculations for Metals and Semiconductors Using a Plane-Wave Basis Set. *Comput. Mater. Sci.* **1996**, *6* (1), 15−50.
(25) Perdew, J.; Burke, L.; Ernzerhof, M. Generalized Gradient Approximation Made Simple. *Phys. Rev. Lett.* **1996**, *77*, 3865.
(26) Emery, A. A.; Wolverton, C. Data descriptor: High-Throughput DFT Calculations of Formation Energy, Stability and Oxygen Vacancy Formation Energy of ABO_3 Perovskites. *Sci. Data* **2017**, *4*, 170153.
(27) Saal, J. E.; Kirklin, S.; Aykol, M.; Meredig, B.; Wolverton, C. Materials Design and Discovery with High-Throughput Density Functional Theory: The Open Quantum Materials Database (OQMD). *JOM* **2013**, *65*, 1501−1509.
(28) Proffen, T.; Page, K. L. Obtaining Structural Information from the Atomic Pair Distribution Function. *Z. Kristallogr. - Cryst. Mater.* **2004**, *219* (3), 130−135.
(29) Aksel, E.; Forrester, J. S.; Nino, J. C.; Page, K.; Shoemaker, D. P.; Jones, J. L. Local Atomic Structure Deviation from Average Structure of $Na_{0.5}Bi_{0.5}TiO_3$: Combined x-Ray and Neutron Total Scattering Study. *Phys. Rev. B: Condens. Matter Mater. Phys.* **2013**, *87* (10), 1−10.
(30) Walsh, A.; Payne, D. J.; Egdell, R. G.; Watson, G. W. Stereochemistry of Post-Transition Metal Oxides: Revision of the Classical Lone Pair Model. *Chem. Soc. Rev.* **2011**, *40* (9), 4455−4463.
(31) Hautier, G.; Ong, S. P.; Jain, A.; Moore, C. J.; Ceder, G. Accuracy of Density Functional Theory in Predicting Formation Energies of Ternary Oxides from Binary Oxides and Its Implication on Phase Stability. *Phys. Rev. B: Condens. Matter Mater. Phys.* **2012**, *85*, 155028.
(32) Yeh, J. W.; Chen, S. K.; Lin, S. J.; Gan, J. Y.; Chin, T. S.; Shun, T. T.; Tsau, C. H.; Chang, S. Y. Nanostructured High-Entropy Alloys with Multiple Principal Elements: Novel Alloy Design Concepts and Outcomes. *Adv. Eng. Mater.* **2004**, *6* (5), 299−303.
(33) Rost, C. M.; Sachet, E.; Borman, T.; Moballegh, A.; Dickey, E. C.; Hou, D.; Jones, J. L.; Curtarolo, S.; Maria, J. P. Entropy-Stabilized Oxides. *Nat. Commun.* **2015**, *6*, 8485.
(34) Martinolich, A. J.; Kurzman, J. A.; Neilson, J. R. Circumventing Diffusion in Kinetically Controlled Solid-State Metathesis Reactions. *J. Am. Chem. Soc.* **2016**, *138* (34), 11031−11037.
(35) Palasyuk, O.; Palasyuk, A.; Maggard, P. A. Site-Differentiated Solid Solution in $(Na_{1-x}Cu_x)_2Ta_4O_{11}$ and its Electronic Structure and Optical Properties. *Inorg. Chem.* **2010**, *49* (22), 10571−10578.
(36) Boltersdorf, J.; Zoellner, B.; Fancher, C. M.; Jones, J. L.; Maggard, P. A. Single- and Double-Site Substitutions in Mixed-Metal Oxides: Adjusting the Band Edges Toward the Water Redox Couples. *J. Phys. Chem. C* **2016**, *120* (34), 19175−19188.
(37) Wu, J; Walukiewicz, W; Yu, K.M; Ager, J.W; Li, S.X; Haller, E.E; Lu, H.; Schaff, W. J Universal Bandgap Bowing in Group-III Nitride Alloys. *Solid State Commun.* **2003**, *127*, 411−414.
(38) Niishiro, R.; Takano, Y.; Jia, Q.; Yamaguchi, M.; Iwase, A.; Kuang, Y.; Minegishi, T.; Yamada, T.; Domen, K.; Kudo, A. A CoO_x-modified $SnNb_2O_6$ photoelectrode for highly efficient oxygen evolution from water. *Chem. Commun.* **2017**, *53*, 629−632.
(39) Zoellner, B.; O'Donnell, S.; Wu, Z.; Itanze, D.; Carbone, A.; Osterloh, F. E.; Geyer, S.; Maggard, P. A. Impact of Nb(V) Substitution on the Structure and Optical and Photoelectrochemical Properties of the $Cu_5(Ta_{1-x}Nb_x)_{11}O_{30}$ Solid Solution. *Inorg. Chem.* **2019**, *58*, 6845.
(40) Kirkpatrick, S. Percolation and Conduction. *Rev. Mod. Phys.* **1973**, *45*, 574.
(41) Shante, K. S.; Kirkpatrick, S. An introduction to percolation theory. *Adv. Phys.* **1971**, *20* (85), 325−357.
(42) Kato, H.; Hori, M.; Konta, R.; Shimodaira, Y.; Kudo, A. Construction of Z-scheme type heterogeneous photocatalysis systems for water splitting into H_2 and O_2 under visible-light irradiation. *Chem. Lett.* **2004**, *33*, 1348−1349.

https://dx.doi.org/10.1021/acs.chemmater.0c00044
Chem. Mater. 2020, 32, 3054−3064